



# Interplanetary Scintillation Observations of Solar-Wind Disturbances During Cycles 23 and 24

Munetoshi Tokumaru<sup>1</sup> · Ken'ichi Fujiki<sup>1</sup> · Kazumasa Iwai<sup>1</sup>

Received: 26 September 2022 / Accepted: 23 January 2023 / Published online: 13 February 2023  
© The Author(s), under exclusive licence to Springer Nature B.V. 2023, corrected publication 2023

## Abstract

Interplanetary scintillation (IPS) analysis is an effective technique for remotely sensing solar-wind disturbances, such as stream-interaction regions (SIRs) and coronal mass ejections (CMEs), which are the main drivers of space weather. Here, we employed 327-MHz IPS observations conducted at the Institute of Space–Earth Environmental Research, Nagoya University for the period of 1997–2019 to determine IPS indices that represent the density-fluctuation level of the inner heliosphere. We then compared these indices with the solar-wind density and speed measured near the Earth. Consequently, we found weak but significant positive correlations between the IPS indices and both the solar-wind density and speed gradient at a time lag of 0 days. This suggests that an increase in IPS indices corresponds to the arrival of the compression region associated with SIR or CME at the Earth, which is consistent with model calculations. Significant negative correlations were observed between the IPS and disturbance storm time (Dst) indices at a time lag of a few days; however, the correlations were too weak to enable reliable predictions of space weather. Possible reasons for these weak correlations are also discussed. Using the IPS indices, we determined the solar-cycle variation in the occurrence rate of solar-wind disturbances for the analysis period. The occurrence rates exhibited two maxima corresponding to the solar maximum and minimum, which are generally consistent with the combined effects of CME and SIR. The lower occurrence rates in Cycle 24 than in Cycle 23 reflect a weaker solar activity. These results suggest that the proposed IPS indices are useful for studying the long-term characteristics of solar-wind disturbances.

**Keywords** Solar wind · Space weather · Solar cycle

## 1. Introduction

The solar wind, which is a turbulent plasma stream emanating from the Sun at a supersonic speed, changes drastically over a wide range of spatial and temporal scales to drive space weather (e.g., Tsurutani, Lakhina, and Hajra, 2020). Accurate information on the solar wind is important for predicting space weather; however, so far, no reliable models have been

---

✉ M. Tokumaru  
tokumaru@isee.nagoya-u.ac.jp

<sup>1</sup> Institute for Space-Earth Environmental Research, Nagoya University, Nagoya, Japan

established to determine solar-wind conditions from observations of the Sun. Therefore, continuous monitoring of the solar wind through either direct or indirect methods is required to predict space weather. In situ observations at the L1 point provide information on the upstream solar wind of the Earth, enabling space-weather predictions approximately 1 h in advance (Zwickl et al., 1998). Interplanetary scintillation (IPS) observations for compact radio sources serve as a useful indirect method for sensing the solar wind from the ground (Hewish, Scott, and Wills, 1964, Coles, 1978) and can provide information on the upstream solar wind one or a few days in advance (e.g., Gapper et al., 1982).

Observations with the Cambridge 81-MHz array first demonstrated the utility of IPS for space-weather predictions (Gapper et al., 1982). In these observations, IPS data were collected for approximately 900 sources per day, and used to calculate the disturbance factor, termed the  $g$ -value, which represents the relative variation of the solar-wind density-fluctuation level ( $\Delta N_e$ ) along the line-of-sight for the region where wave scattering is weak. Solar-wind disturbances between the Sun and Earth orbit were clearly revealed from a series of all-sky maps of the  $g$ -values produced on a daily basis. The utility of IPS, particularly for studying coronal mass ejections (CMEs), has been further explored through subsequent observations in India, Russia, and Japan (Manoharan, 1997, 2006, 2010, Chashei et al., 2016, Tokumaru et al., 2000b, 2003, 2005, 2006a,b, 2007, 2019). CMEs are regarded as one of the primary targets in space-weather predictions, because fast CMEs associated with the southward component of the interplanetary magnetic field (IMF) are likely to cause intense geomagnetic storms (Tsurutani, Lakhina, and Hajra, 2020). When the line-of-sight for an IPS source intersects the compression region driven by a CME, the  $g$ -value increases above unity. The magnitude of increased  $g$ -values and their distribution in the sky map indicate the  $\Delta N_e$  level and global structure of CME, respectively. Increased  $g$ -values detected from IPS observations have been analyzed to determine the three-dimensional properties and propagation dynamics of CMEs in the solar wind (e.g., Tokumaru et al., 2003, 2006a,b, 2007). However, not all CMEs are necessarily associated with the compression region; that is, slow CMEs are unlikely to drive the compression region in the solar wind, and  $g$ -value measurements preferentially detect fast CMEs. The  $g$ -value measurements are also useful for observing corotating plasma streams (Houminer, 1971; Tappin, Hewish, and Gapper, 1984). Although  $g$ -value data are useful for detecting and tracking solar-wind disturbances for specific events, few studies have examined the long-term properties of solar-wind disturbances using  $g$ -values. This is primarily attributed to a lack of freely available  $g$ -value data that covers a long period, e.g., more than one solar cycle. At present,  $g$ -value data that cover two solar cycles, i.e., Cycles 23 and 24, are available from 327-MHz IPS observations at the Institute for Space-Earth Environmental Research (ISEE) of Nagoya University (Tokumaru, 2013).

In this study, we analyzed ISEE  $g$ -value data to determine the long-term properties of solar-wind disturbances. Specifically, IPS indices derived from  $g$ -values on a daily basis were employed as an indicator of solar-wind disturbances. These IPS indices are useful for comparison with in situ measurements and geomagnetic indices (Harrison et al., 1992; Hapgood and Harrison, 1994), and for evaluating long-term variations of solar-wind disturbances. Different types of IPS indices, such as INDEX35 ( $I_{35}$ ),  $I_{hi}$ , and  $G_{ave}$  have been proposed via a series of pioneering studies using Cambridge IPS observations (Harrison et al., 1992; Lucek and Rodger, 1995; Lucek, Clark, and Moore, 1996). The former two indices are defined as follows:

$$I_{35} = \frac{GT - LT}{N} \quad (1)$$

$$I_{hi} = \frac{GT'}{N}, \quad (2)$$

where  $GT$  and  $LT$  are the numbers of sources with  $g > 1.35$  and  $g < 0.65$ , respectively,  $N$  is the total number of sources, and  $GT'$  is the number of sources with  $g > 1.4$  (Harrison et al., 1992; Lucek and Rodger, 1995). The index  $G_{ave}$  is the daily average of  $g$ -values. We note that various threshold levels for  $I_{hi}$  were examined in a subsequent study (Lucek, Clark, and Moore, 1996). According to a comparison between IPS and geomagnetic Ap indices during the period 1990–1992, positive correlations with coefficients of 0.4–0.5 were found for most cases, with a lag of either +1 day or zero lag (Lucek, Clark, and Moore, 1996). In this study, we calculated  $I_{50}$ , which is defined in a similar way to  $I_{35}$ , as well as  $I_{hi}$  and  $G_{ave}$  from ISEE IPS observations for 1997–2019. We then compared these indices with solar-wind density and speed observed near the Earth, as well as with the geomagnetic-disturbance storm time (Dst) indices. Although  $I_{35}$ ,  $I_{hi}$ , and  $G_{ave}$  gave results similar to each other in the earlier study (Lucek, Clark, and Moore, 1996), the latter two indices yielded a slightly better correlation coefficient with geomagnetic indices at a lag of +1 day than that obtained using  $I_{35}$ ; therefore, the three types of IPS indices are examined separately in this study. ISEE IPS observations have an advantage over Cambridge IPS observations in that they are less affected by ionospheric effects: Cambridge IPS observations were sometimes seriously contaminated by ionospheric disturbances (Lucek and Rodger, 1995), whereas such contamination is rare for ISEE IPS observations because the observation frequency is approximately four times higher than that of the Cambridge IPS observations.

Next, we determined the disturbance event days based on the IPS indices, and calculated the annual occurrence rates of disturbance event days for the Solar Cycles (SCs) 23 and 24. We noted that there were two causes of solar-wind disturbances identified by the IPS indices; one is a fast CME, as mentioned above, and the other is high-speed solar-wind streams, which are another driver of intense geomagnetic storms (Tsurutani, Lakhina, and Hajra, 2020). Both are associated with compressed plasma at the leading portion, which may increase the  $g$ -value when the line-of-sight intersects. The compression region driven by the high-speed stream is termed the stream-interacting region (SIR), or corotating interaction region (CIR) when it survives over multiple solar rotations (Gosling and Pizzo, 1999; Richardson, 2018). The formation of a SIR or CIR may be possible at distances close to the Earth's orbit, although how it evolves with radial distance is still largely unknown (e.g., Jian et al., 2008; Allen et al., 2021). If the scale of the compression region associated with the CME or SIR/CIR is large enough to produce increases in  $g$ -value for the majority of radio sources observed in a given day, solar-wind disturbances are identified by an increase in the value of IPS indices. Furthermore, periodic variations in the IPS indices are likely to be observed for the case of CIR.

The remainder of this article is organized as follows. Section 2 provides a concise description of the ISEE IPS observations, the IPS indices, near-Earth in situ data and Dst index data used in this study. Section 3 presents the analysis results, which include a comparison with in situ and geomagnetic data and long-term variations of solar-wind disturbances. In addition, we perform wavelet analysis of the IPS indices to detect the effect of CIR. In Section 4, model calculations of the  $g$ -value are presented to explain the results. In Section 5, we discuss the implications and contributions of our findings.

## 2. Observations and Data

### 2.1. IPS Observations

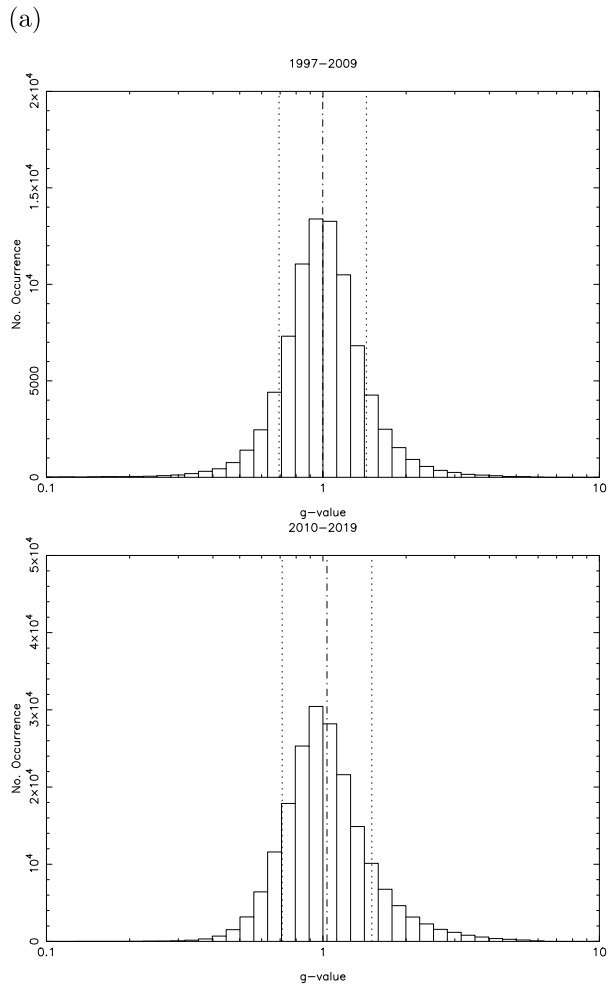
IPS observations of the solar-wind speed have been performed regularly at ISEE since the early 1980s using the 327-MHz multistation system, which is composed of three or four large-aperture radio telescopes (Kojima and Kakinuma, 1990; Tokumaru, 2013). The corresponding  $g$ -value data have been made available since 1997 (Tokumaru et al., 2000b). The  $g$ -value is the ratio of the IPS level  $\Delta I$  observed for a given source and time to the smoothed curve of IPS variations  $\overline{\Delta I(R)}$  that is defined as a function of the radial distance  $R$ :

$$g = \frac{\Delta I}{\overline{\Delta I(R)}}, \quad (3)$$

where  $R$  is given as  $R = 1 \text{ AU} \times \sin \varepsilon$  and  $\varepsilon$  is the solar-elongation angle. The value of  $\Delta I$  is calculated from power-spectrum analysis of IPS data collected at a single station, and  $\overline{\Delta I(R)}$  is determined by fitting a power-law function of  $aR^b$  to  $\Delta I$  observations in a year. The typical range of observed  $b$  is between  $-1$  and  $-2$ , and it tends to be flatter (steeper) at solar minimum (maximum; Tokumaru et al., 2000a). The  $\Delta I$  observed at  $R$  is normalized by  $\overline{\Delta I(R)}$  to determine the  $g$ -value. Here, it should be noted that the  $g$ -value serves as a measure of  $\Delta N_e$  in the weak-scattering region. At 327 MHz, the transition from weak to strong scattering occurs at  $\varepsilon$  of approximately  $11^\circ$ , i.e.,  $R \simeq 0.2 \text{ AU}$  for the undisturbed solar wind. Therefore, the estimation of the  $g$ -value is valid only for  $R > 0.2 \text{ AU}$ . Furthermore, the dynamic range of the  $g$ -value depends on  $R$ , and it is greatly limited at solar offsets close to the transition distance: the increase in  $g$ -value is suppressed by the effect of the weak-to-strong transition when the line-of-sight is located near  $0.2 \text{ AU}$  (Tokumaru et al., 2005). The  $g$ -value was calculated for  $R > 0.2 \text{ AU}$  using IPS data collected by the Kiso antenna prior to 2009, and the Toyokawa antenna after 2010 (Tokumaru et al., 2011). Since ISEE IPS observations are collected for  $\varepsilon < 90^\circ$ , the radial distance range covered by the  $g$ -value data is between  $0.2 \text{ AU}$  and  $1 \text{ AU}$ . All  $g$ -value data from ISEE IPS observations are available online via the web site (<https://stsw1.isee.nagoya-u.ac.jp/vlist/g/>). We note that the  $g$ -value data for SC23 are unavailable during winter because the Kiso antenna ceases to function in the snow. In contrast, the  $g$ -value data for SC24 are available throughout the year because observations at Toyokawa are not interrupted by snow.

Figure 1 shows histograms of the  $g$ -values for (a) 1997–2009 (SC 23) and (b) 2010–2019 (SC 24), which correspond to the data derived from IPS observations with the Kiso and Toyokawa antennas, respectively. Both datasets exhibit log-normal distributions centered at  $g = 1$  with an almost identical width of the distribution. The  $+1\sigma$  deviations from the mean are 1.44 and 1.45 for (a) and (b), respectively. The distributions of the two datasets are similar, implying homogeneity of the  $g$ -value datasets. However, the number of  $g$ -values available in a day differs between the two datasets. According to Figure 2, the average daily number of  $g$ -values for SC23 is approximately 30 until 2005, decreasing gradually thereafter. This decline in the number of daily  $g$ -values is mostly attributed to degradation of the system sensitivity. In contrast, the number of daily  $g$ -values for SC24 is over 40 between 2010 and 2014, then increases to 60 in 2015. This larger daily number of  $g$ -values is attributed to the short beam-switching time and high sensitivity of the Toyokawa antenna, which enables IPS observations for more radio sources per day as well as optimization of the observation schedule. Thus, the daily numbers of  $g$ -values for SC24 are approximately 1.5 or 2 times higher than those for SC23.

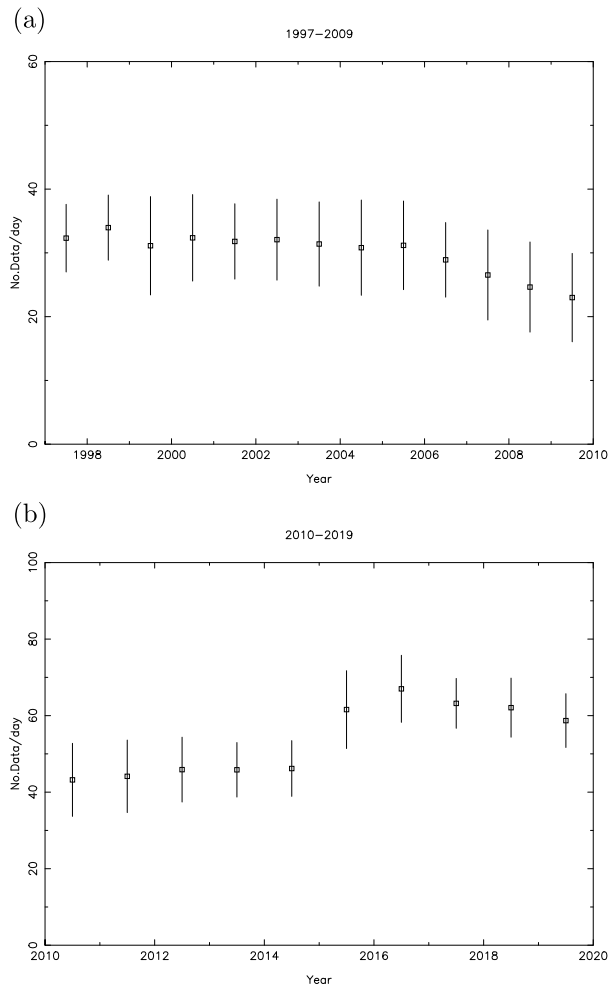
**Figure 1** Histograms of  $g$ -values derived from ISEE IPS observations for (a) 1997–2009 and (b) 2010–2019. Dot-dashed and dotted lines indicate the average and  $\pm 1\sigma$  values in log space.



## 2.2. IPS Indices

The  $g$ -value represents the weighted integration of  $\Delta N_e$  along the line-of-sight, where  $g = 1$  corresponds to a quiet (i.e., undisturbed) solar wind. When high- $\Delta N_e$  plasma driven by the interaction with either fast CMEs or high-speed solar wind intersects the line-of-sight, the  $g$ -value increases to more than unity. The magnitude of increased  $g$ -values and the number of lines-of-sight showing increases in  $g$ -value are regarded as key parameters for evaluating the importance of solar-wind disturbances. The IPS indices mentioned above are determined from these parameters. In this study, we calculated three types of IPS indices  $I_{50}$ ,  $I_{hi}$ , and  $G_{ave}$  from the  $g$ -value data. The index  $I_{50}$  is a modified version of  $I_{35}$ . The threshold levels of  $I_{50}$  for high or low scintillation are different from those of  $I_{35}$ : 1.50 or 1/1.50 for  $I_{50}$ . These threshold levels correspond to  $\pm 1\sigma$  deviation (vertical dotted lines in Figure 1). The threshold level for  $I_{hi}$  is defined as 1.50 ( $+1\sigma$  from 1) in this study. The minimum number of  $g$ -values required to calculate the IPS indices was set to 10 in this study. The total number of the days when IPS indices were available were 2691 and 3598 for SC23 and SC24, respectively.

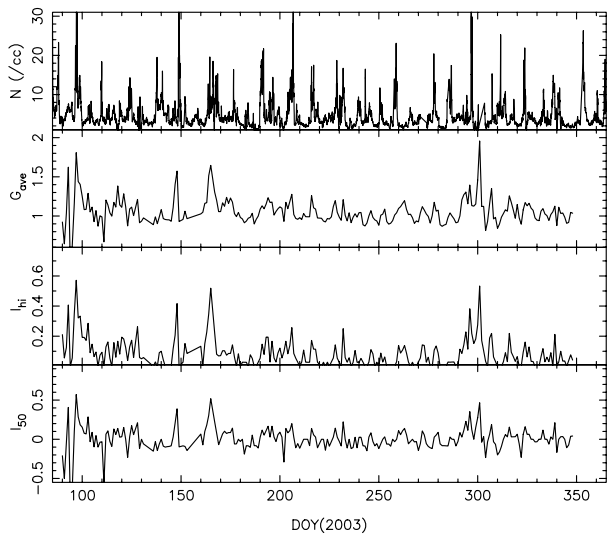
**Figure 2** Mean number of  $g$ -values available per day for the periods of (a) 1997–2009 and (b) 2010–2019. Vertical bars on each data point indicate  $\pm 1\sigma$  of the mean.



### 2.3. In Situ Observations of the Solar-Wind and Dst-Index Data

The IPS indices were compared with data of the solar-wind density and speed observed in situ near the Earth. The hourly averaged solar-wind data were obtained from the OMNI dataset of NASA/GSFC through OMNIweb (<https://omniweb.gsfc.nasa.gov/>), and the daily averaged data were derived from the hourly OMNI data for comparison with the IPS indices. We also compared the IPS indices with the Dst index, which is calculated from magnetic-field observations at low-latitude stations. This index decreases as the ring current develops in the Earth's magnetosphere, and serves as a reliable indicator for the occurrence of geomagnetic storms (Sugiura, 1964). Hourly Dst-index data were downloaded from the web site of the World Data Center for Geomagnetism, Kyoto (<https://wdc.kugi.kyoto-u.ac.jp/index.html>). Daily average values of Dst index were calculated for comparison with the IPS indices.

**Figure 3** Temporal variation of (from bottom to top)  $I_{50}$ ,  $I_{hi}$ ,  $G_{ave}$ , and solar-wind density  $N$  for 2003.



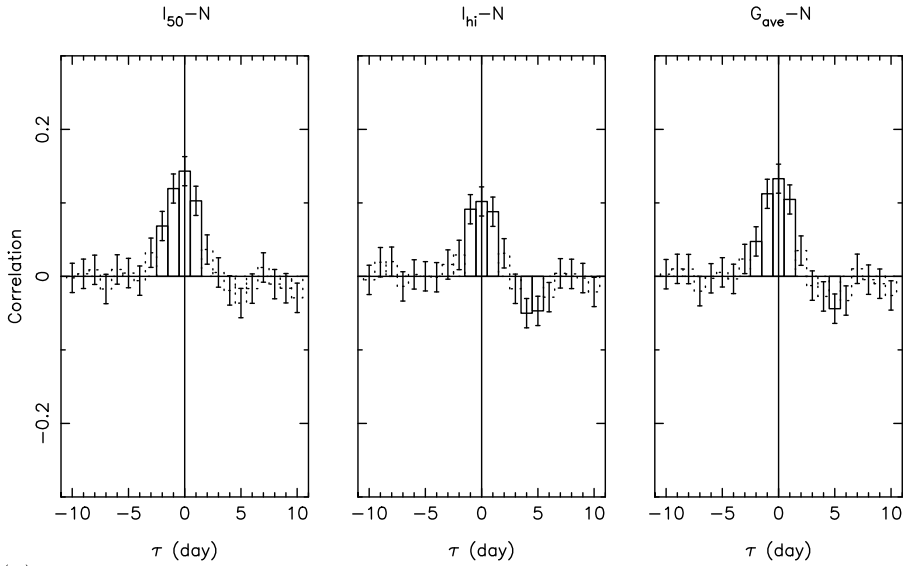
### 3. Results

#### 3.1. Comparison with Solar-Wind Density

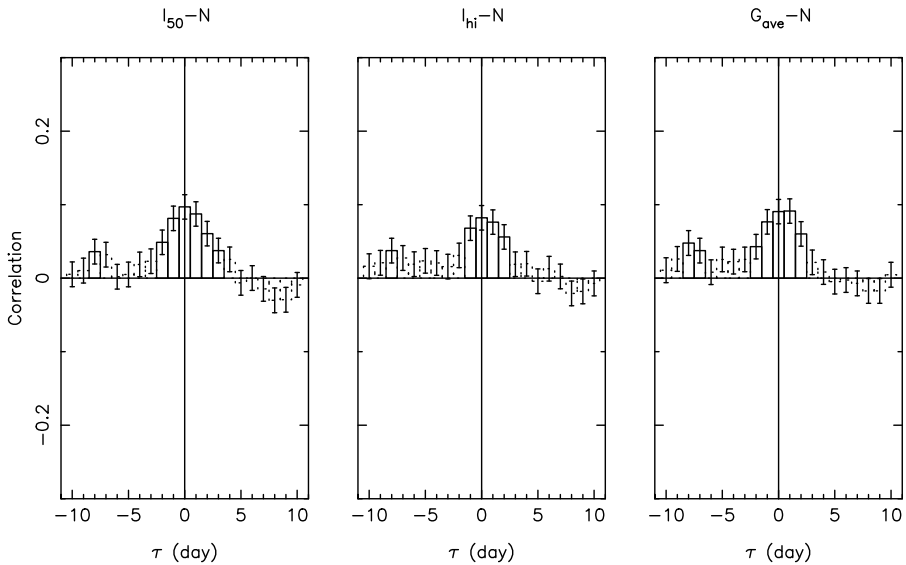
The three IPS indices  $I_{50}$ ,  $I_{hi}$ ,  $G_{ave}$ , and the hourly averaged solar-wind density  $N$  for 2003 are plotted as a function of time in Figure 3. The IPS indices show similar temporal variations, including sporadic increases, which suggest the occurrence of solar-wind disturbances. Many peaks are also discernible in the plot of solar-wind density, although only some of which are associated with increases in IPS indices.

Figure 4 shows the crosscorrelations between the IPS indices and  $N$  for (a) SC23 and (b) SC24. The correlation coefficients are plotted as a function of time lag  $\tau$ . We also calculated the standard errors and  $p$ -values of the observed correlation coefficients for each bin of the time lag. The bins drawn by solid lines indicate statistically significant correlations for which the null hypothesis is rejected with a significance level of 0.05, i.e.,  $p < 0.05$ . The vertical bars on the top of each bin represent the standard errors. As seen in the figure, all IPS indices show weak positive correlations with coefficients of 0.1–0.15 at around zero lag. Although there is no significant difference in correlations between the three IPS coefficients, the coefficients observed for SC24 are consistently smaller than those for SC23. Figure 5 shows the annual variation in the maximum correlation coefficients between the IPS indices and  $N$  for (a) SC23 and (b) SC24. The monthly averaged sunspot numbers obtained from the World Data Center (WDC) Sunspot Index and Long-term Solar Observations (SILSO) are also plotted in the figure. Weak but significant positive correlations are observed throughout both SCs, and most of the maximum correlation coefficients occur at a time lag of  $\tau = 0$  day. Although some of the variations are within the standard errors, the solar-cycle dependence of these correlations is still seen in this figure, that is, consistently higher coefficients beyond the standard errors are observed near the solar maxima. The variations in the maximum correlation coefficients do not exactly follow those of the sunspot number, with the highest correlation observed in 2003 for SC23 and 2013 for SC24.

(a)



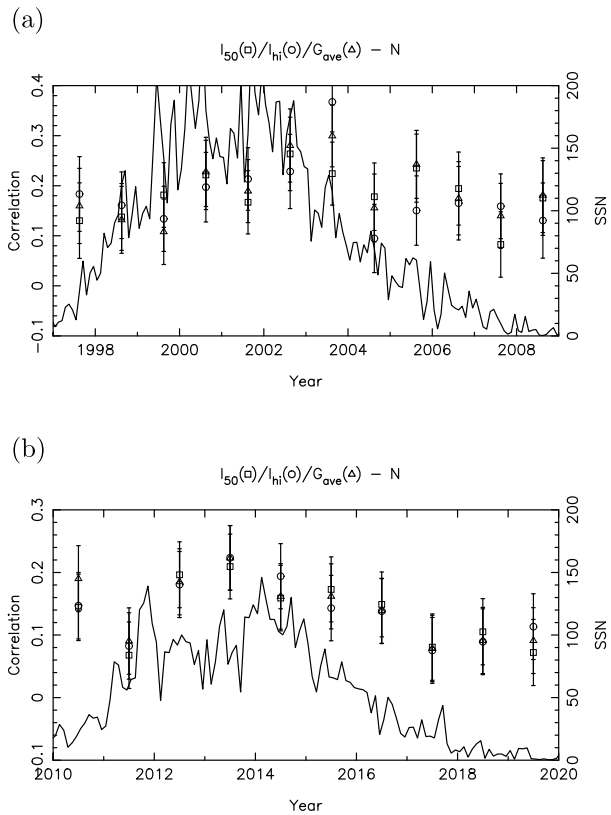
(b)



**Figure 4** Crosscorrelation coefficients between (left to right)  $I_{50-N}$ ,  $I_{hi-N}$ , and  $G_{ave-N}$  for (a) 1997–2009 and (b) 2010–2019, plotted as a function of the time lag to the IPS indices. Bins drawn by solid (dotted) lines denote  $p$  values less (greater) than 0.05. Vertical bars on each bin indicate the standard error of the correlation coefficient.



**Figure 5** Temporal variation of maximum correlation coefficients between the IPS indices and  $N$  (symbols), and the monthly averaged sunspot numbers SSN (solid line) for (a) 1997–2009 and (b) 2010–2019. Squares, circles, and triangles denote  $I_{50}$ ,  $I_{hi}$ , and  $G_{ave}$ , respectively. Vertical bars on the data points indicate the standard error of the correlation coefficient.



### 3.2. Comparison with Solar-Wind Speed

Figure 6 shows the crosscorrelations between the IPS indices and solar-wind speed  $V$  for (a) SC23 and (b) SC24. Weak but significantly positive correlations occur between the IPS indices and  $V$  for SC23 at a time lag of  $\tau = +1$  or  $+2$  days. Unlike the almost symmetrical peaks of positive correlations found for  $N$ , the shape of the positive correlations for  $V$  is asymmetric, comprising a sharp rise at zero lag and a gradual fall during the subsequent five days. These results clearly suggest that increased  $g$ -values correspond to the leading edge of the fast solar wind. The magnitude of positive correlations with solar-wind speed is approximately 0.1, which is almost the same as that for  $N$ . Another interesting aspect revealed in Figure 6(a) is the weak negative correlations for  $\tau = -3 \sim -1$ , although they are not significant for  $I_{hi}$ ; i.e.,  $p > 0.05$ . These negative correlations are attributed to the slow solar wind preceding the fast solar wind. In contrast, no significant positive correlations are observed for SC24 at  $\tau > 0$ , although slight increases in the coefficient with  $p > 0.05$  are revealed for  $I_{50}$  and  $G_{ave}$  at  $\tau > 0$ , as shown in Figure 6(b). Instead, significant negative correlations at  $\tau < 0$  are more prominent for SC24 than for SC23. These negative correlations apply to all IPS indices, and their magnitudes increase as  $\tau$  changes from  $-5$  to  $-1$  day. The maximum negative correlation occurs at  $\tau = -1$  day. Significant negative correlations are still observed at  $\tau = 0$ , but disappear for  $\tau > 0$ . This suggests that the increases in  $g$ -value observed for SC24 are closely associated with the preceding slow solar wind. We consider that increases in  $g$ -value represent the leading edge of the fast solar wind, where the speed

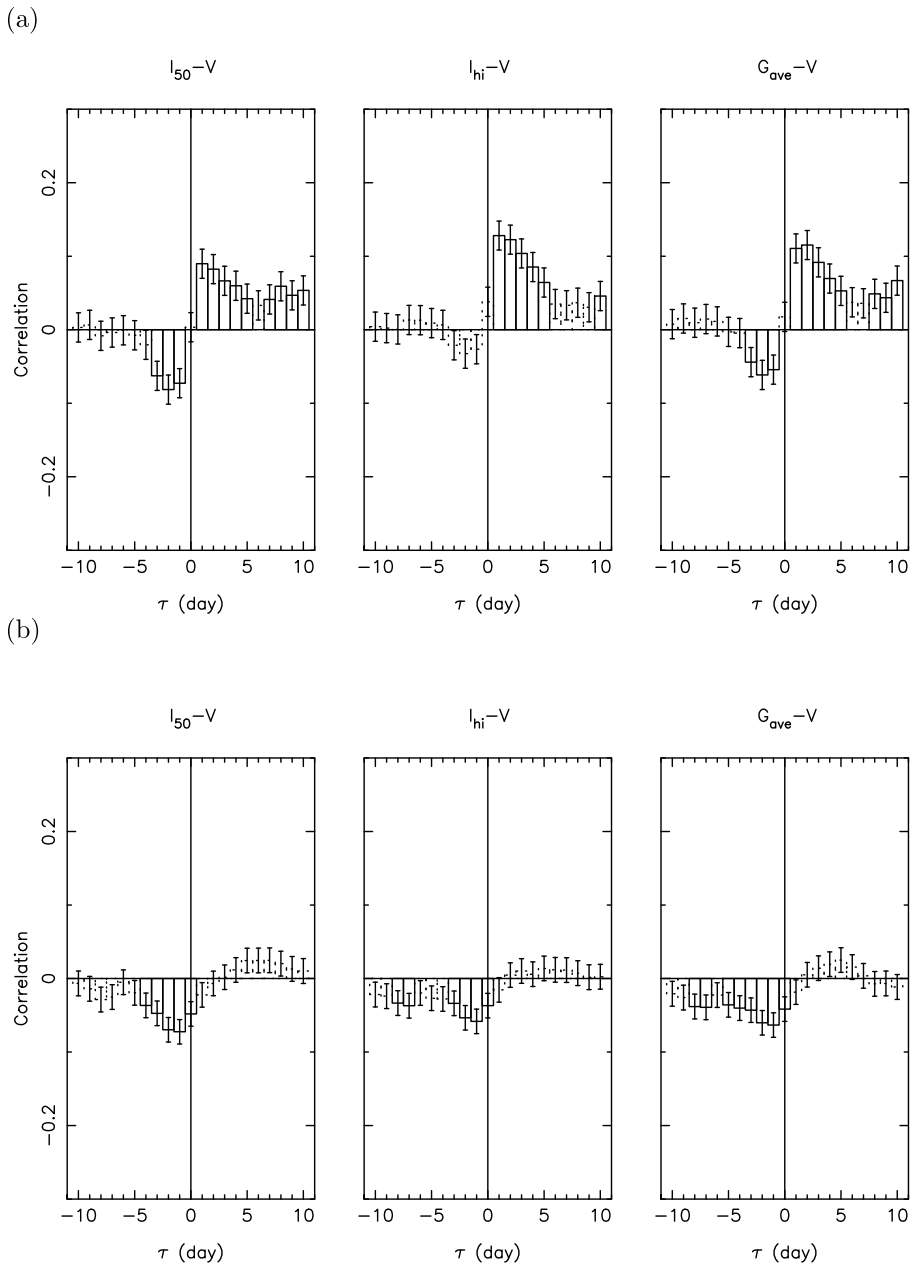


**Figure 6** Crosscorrelation coefficients between (left to right)  $I_{50}-V$ ,  $I_{hi}-V$ , and  $G_{ave}-V$  for (a) 1997–2009 and (b) 2010–2019 plotted as a function of the time lag to the IPS indices. Bins drawn by solid (dotted) lines denote  $p$  values less (greater) than 0.05. Vertical bars on each bin indicate the standard error of the correlation coefficient.

gradient generates compressed plasma. To examine this hypothesis, we calculated the speed gradients  $dV/dt$  from the in situ data, and compared them with the IPS indices. Figure 7 shows the crosscorrelations between IPS indices and  $dV/dt$  for (a) SC23 and (b) SC24. Sharp peaks of positive correlations at zero lag are revealed for both SC23 and SC24. Although the peak correlations for SC24 are rather small, they are still significant ( $p < 0.05$ ), supporting the aforementioned interpretation.

Figure 8 shows the annual variations in the maximum correlation coefficients between the IPS indices and  $dV/dt$  for (a) SC23 and (b) SC24, respectively. Positive correlations with magnitudes of 0.1–0.2 are observed throughout the analysis period, with weaker correlations for SC24 than for SC23. Relatively high correlation coefficients for SC23 are observed for the period between the solar maximum and the early declining phase, i.e., the largest positive correlation occurs in 2000, and the second largest occurs in 2003. These increases are considered significant as compared with the standard errors. In contrast, the largest positive correlation for SC24 occurs at the solar minimum between SC23 and SC24, i.e., 2010, whereas the secondary peak occurs near the solar maximum, i.e., 2014. These features are generally consistent with those of the correlation between IPS indices and  $N$  (Figure 5). However, the change in correlation coefficients observed for SC24 is within the standard errors, and therefore we cannot say for certain that it is significant.

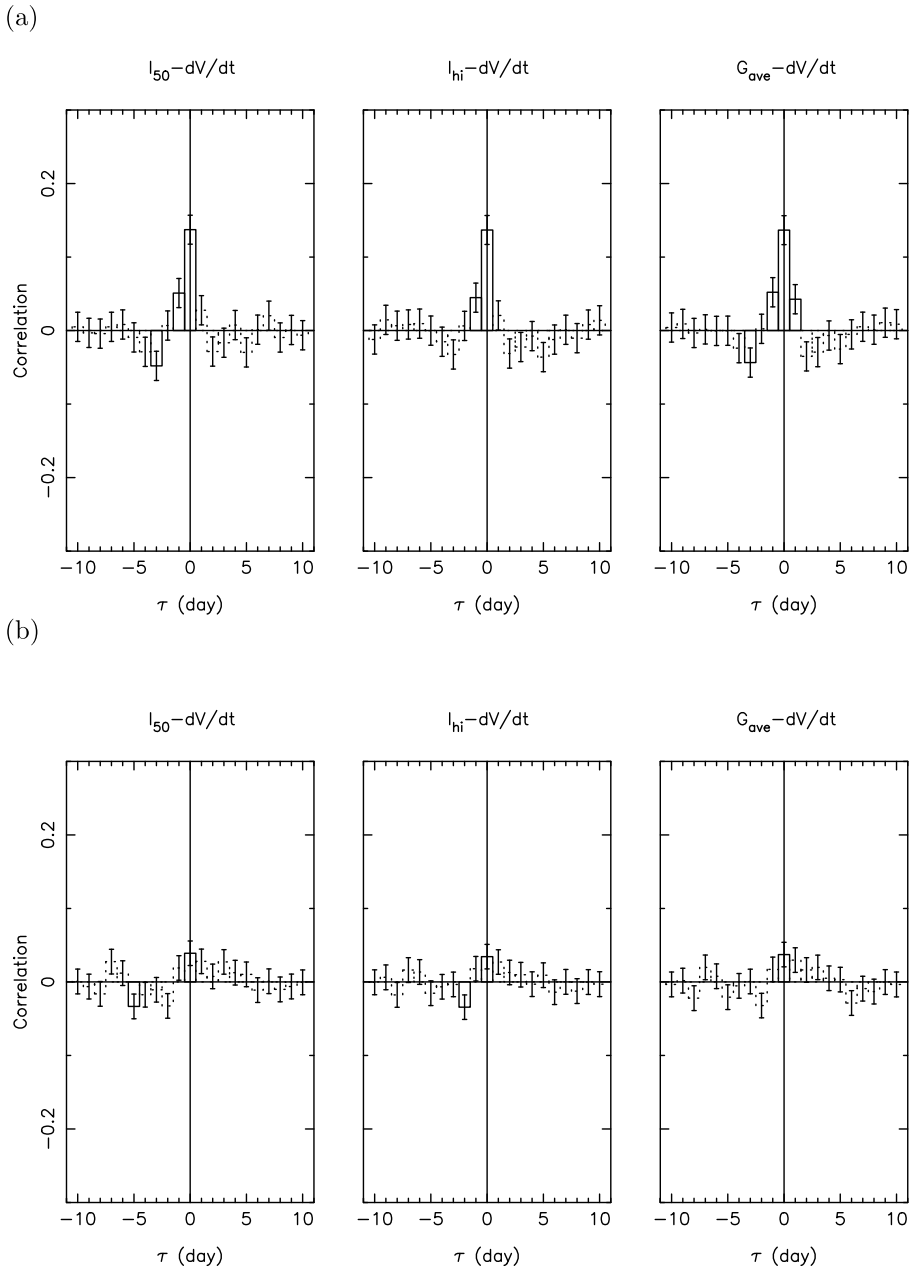
### 3.3. Comparison with the Dst Index

The correlation coefficients between IPS and Dst indices are plotted in Figure 9 as a function of  $\tau$  for (a) SC23 and (b) SC24. Significant negative correlations are observed at a positive time lag for SC23. The coefficients abruptly drop to a negative peak value ( $\sim -0.15$ ) at  $\tau = +1$  days, before gradually returning to close to zero. In contrast, positive correlations occur at  $\tau = -2 \sim -1$  days for SC24, whereas the negative correlations at a positive time lag are weaker and less distinct for SC24 than for SC23. These results suggest that increased IPS indices may serve as precursors of geomagnetic disturbances driven by solar-wind disturbances; however, the correlations are too weak to make a reliable prediction.

Figure 10 shows the annual variations in the negative correlations at the time lags with the maximum magnitudes for (a) SC23 and (b) SC24. The magnitudes of the negative correlations increase in the period between the solar maximum and the declining phase of SC23, with relatively strong negative correlations observed in 2000, 2003, and 2004. These are considered significant increases, because their changes are larger than the standard errors. The correlation observed for 2014 (SC24 maximum) is relatively strong, but this change is insignificant. The correlation coefficients between the IPS and Dst indices exhibit greater variation than those between the IPS indices and  $N$  or  $V$ . The main reason for this is the complex coupling processes between the solar wind and the magnetosphere that are involved in the occurrence of geomagnetic storms. The IPS observations do not provide information on the IMF, particularly for the north–south component of IMF ( $B_z$  component), which is known to strongly control solar-wind–magnetosphere coupling (Tsurutani et al., 1988; Tsurutani, Lakhina, and Hajra, 2020). Nevertheless, it is noteworthy that significant correlations occur between IPS and Dst indices.

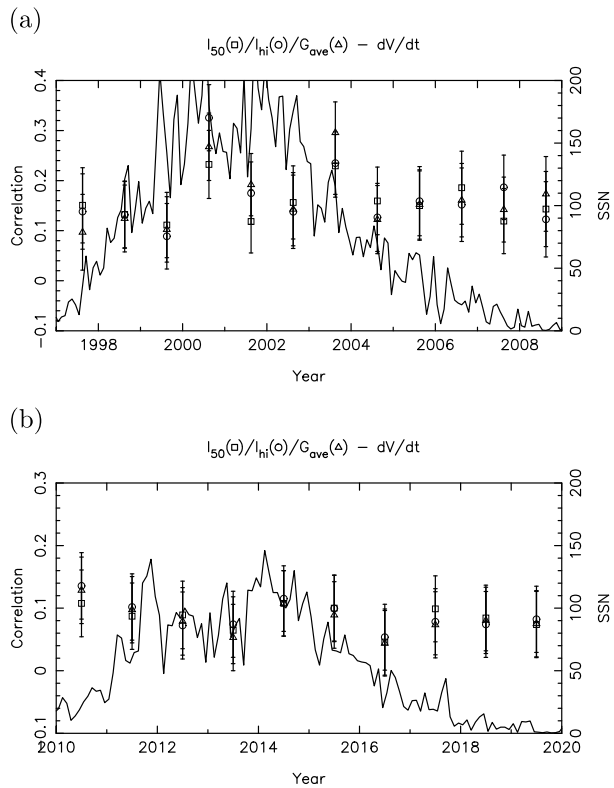
### 3.4. Occurrence Rates of Solar-Wind Disturbances

The occurrence rate of solar-wind disturbances for a given year is determined by counting the day when the IPS index exceeds a certain threshold level. The threshold level is determined from the average value and the rms deviation ( $\sigma$ ) of each IPS index over the period of



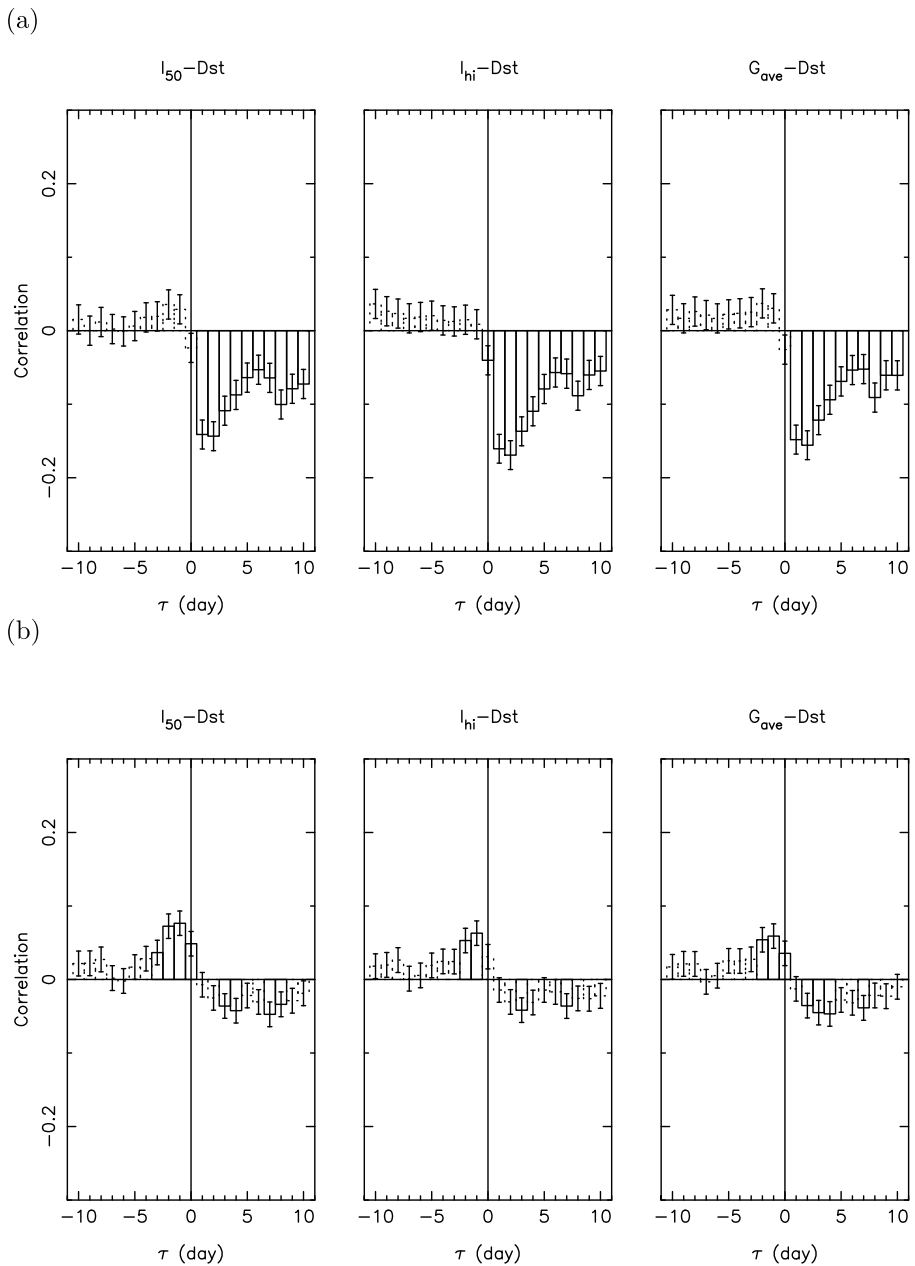
**Figure 7** Crosscorrelation coefficients between (left to right)  $I_{50}-dV/dt$ ,  $I_{hi}-dV/dt$ , and  $G_{ave}-dV/dt$  for (a) 1997–2009 and (b) 2010–2019, plotted as a function of the time lag to the IPS indices. Bins drawn by solid (dotted) lines denote  $p$  values less (greater) than 0.05. Vertical bars on each bin indicate the standard error of the correlation coefficient.

**Figure 8** Temporal variation of maximum correlation coefficients between the IPS indices and  $dV/dt$  (symbols), and the monthly averaged sunspot numbers SSN (solid line) for (a) 1997–2009 and (b) 2010–2019. Squares, circles, and triangles denote  $I_{50}$ ,  $I_{hi}$ , and  $G_{ave}$ , respectively. Vertical bars on the data points indicate the standard error of the correlation coefficient.



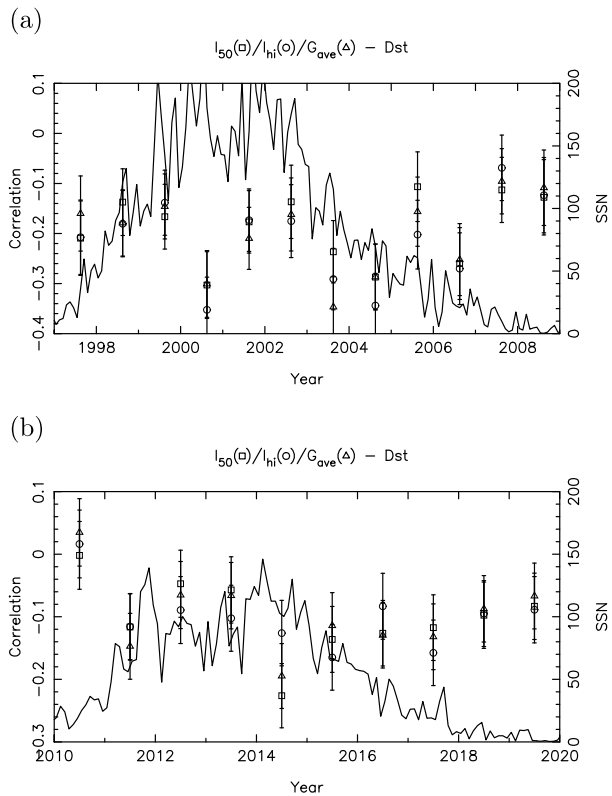
either SC23 or SC24. The monthly average IPS indices show no significant changes during the solar cycle, despite the drastic variation of solar activity during the analysis period. This validates the use of a single threshold level for detecting solar-wind disturbances from IPS indices throughout the solar cycle. The threshold level is given as the average plus  $1\sigma$  for each IPS index, i.e.,  $I_{50} = 0.173$ ,  $I_{hi} = 0.204$ , and  $G_{ave} = 1.255$  for SC23 and  $I_{50} = 0.164$ ,  $I_{hi} = 0.219$ , and  $G_{ave} = 1.268$  for SC24.

Figure 11 shows the annual variations in the occurrence rate of solar-wind disturbances for (a) SC23 and (b) SC24. The three IPS indices yield generally consistent occurrence rates, although  $I_{50}$  tends to be slightly higher than the others. As demonstrated in the figure, the occurrence rates vary with the SC, i.e., the occurrence rates for SC23 are lowest in 2004 (declining phase) and highest in 2009 (solar minimum between SC23 and SC24). Other increases in the occurrence rate are observed in 1999 and 2001 (solar maximum). In contrast, the occurrence rates for SC24 are higher between the SC23/24 minimum and the rising phase, then drop at the solar maximum. The occurrence rates gradually rise again in the declining phase of SC24, reaching a peak at the next solar minimum. The highest rate is observed in 2011 (rising phase), whereas the lowest occurs in 2014 (maximum). A secondary maximum of the occurrence rates occurs in 2019 (SC24/SC25 solar minimum). The occurrence rates in 2009 are consistent with those in 2010, although different systems were used for the IPS observations, which suggests uniformity of the data used in this study. The temporal variation of the occurrence rate revealed in Figure 11 is ascribed to the combination of CME and high-speed solar-wind effects. The former is considered to be more predominantly responsible than the latter for the increased occurrence rates at the SC23 so-



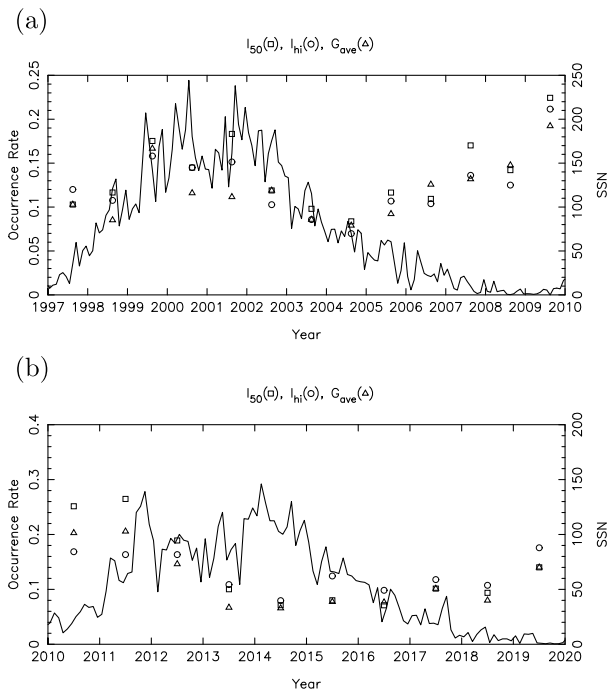
**Figure 9** Crosscorrelation coefficients between (left to right)  $I_{50}$ -Dst,  $I_{hi}$ -Dst, and  $G_{ave}$ -Dst for (a) 1997–2009 and (b) 2010–2019, plotted as a function of the time lag to the IPS indices. Bins drawn by solid (dotted) lines denote  $p$  values less (greater) than 0.05. Vertical bars on each bin indicate the standard error of the correlation coefficient.

**Figure 10** Temporal variation of the maximum amplitudes of the negative correlations between IPS indices and Dst (symbols) and monthly averaged sunspot numbers SSN (solid line) for (a) 1997–2009 and (b) 2010–2019. Squares, circles, and triangles denote  $I_{50}$ ,  $I_{hi}$ , and  $G_{ave}$ , respectively. Vertical bars on the data points indicate the standard error of the correlation coefficient.



lar maximum. The number of interplanetary counterparts of CME (ICMEs) observed near the Earth prominently peaked at the SC23 solar maximum, whereas the number of high-speed solar winds did not follow the variations in the sunspot number (Richardson and Cane, 2010; Grandin, Aikio, and Kozlovsky, 2019). The lower occurrence rate at the SC24 solar maximum is consistent with a smaller number of near-Earth ICME events, which is ascribed to weaker solar activity during this cycle (Grandin, Aikio, and Kozlovsky, 2019). Notably, the local minimum of the occurrence rates observed in 2014 is in good agreement with the yearly distribution of high-speed solar-wind events in SC24 (Gerontidou, Mavromichalaki, and Daglis, 2018; Grandin, Aikio, and Kozlovsky, 2019; Besliu-Ionescu, Maris Muntean, and Dobrica, 2022). Thus, the temporal variation in the occurrence rates for SC24 is likely dominated by the high-speed solar-wind events given the fewer occurrences of CMEs. The local minimum in the occurrence rates observed in 2004 is probably due to the combined effect of CME and high-speed solar-wind events; the number of the former rapidly decreases after the SC23 solar maximum, whereas the latter gradually increases as the solar activity declines, and the year of 2004 corresponds to a plateau in the increasing trend of yearly distribution of high-speed solar-wind events (Grandin, Aikio, and Kozlovsky, 2019). On the other hand, a marked growth of the occurrence rates observed at the SC23/24 solar minimum cannot be fully explained by the combined effects of ICME and high-speed solar-wind events. Although the number of high-speed solar winds greatly increased during 2006–2008, it dropped in 2009, showing a local minimum (Grandin, Aikio, and Kozlovsky, 2019).

**Figure 11** Temporal variation of the occurrence rates of solar-wind disturbances determined by IPS indices (symbols) and monthly averaged sunspot numbers SSN (solid line) for (a) 1997–2009 and (b) 2010–2019: squares, circles, and triangles correspond to the data of  $I_{50}$ ,  $I_{hi}$ , and  $G_{ave}$ , respectively.

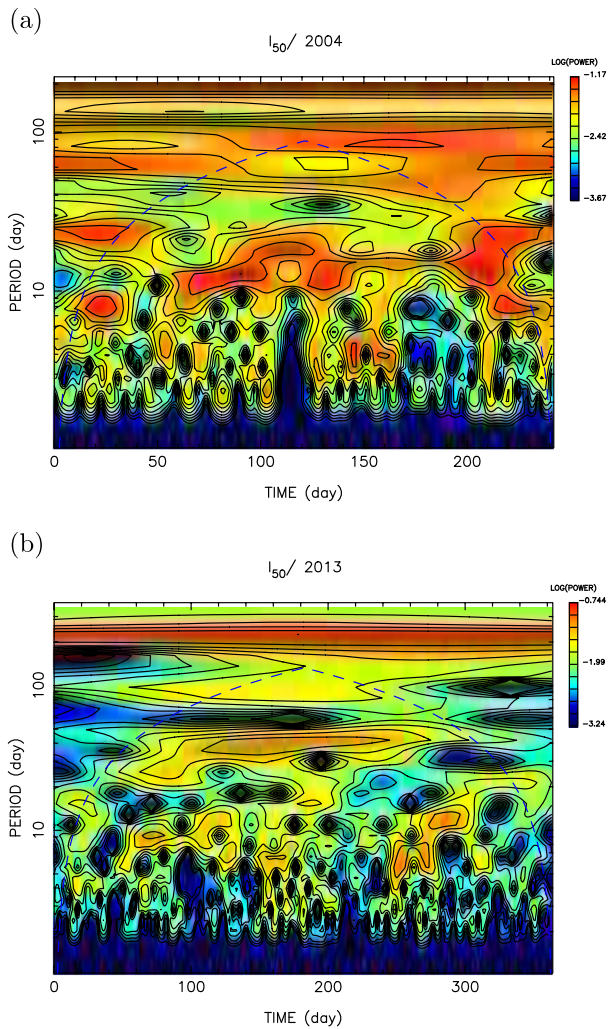


### 3.5. Wavelet Analysis of IPS Indices

Here, we calculate the wavelet power spectra of the IPS indices for each year. For this analysis, data gaps caused by interruptions in the IPS observations were linearly interpolated. Figure 12 shows the wavelet spectra of  $I_{50}$  for (a) 2004 and (b) 2013. Note that the spectra for  $I_{hi}$  and  $G_{ave}$  are similar, with no significant differences among the three indices. In Figure 12(a), a component with a period of  $\sim 15$  days is observed between days 50 and 150. This periodicity corresponds to approximately one-half of the solar-rotation period as viewed from the Earth. A periodic component is also found in Figure 12(b), but the period is approximately equal to the solar rotation period of 27 days. Such a periodic component was identified in the early declining phases of both SC23 and SC24, as well as in the rising phase of SC23. This is consistent with the fact that the SIR/CIR develops during the rising and declining phases of the cycle, owing to the equatorward extension of polar coronal holes. If the CIRs develop at multiple longitudes during one rotation, a periodicity of less than 27 days is likely to be observed in the IPS indices. A periodicity of 15–30 days is not clearly discernible in the solar minima of SC23 and SC24, i.e., 2008, 2009, 2018, and 2019. Furthermore, we note that significant data gaps were present in the central portion of the time-series data for 2008 and 2009. This may explain the lack of periodicity for these years, as opposed to an intrinsic effect.



**Figure 12** Wavelet power spectra of  $I_{50}$  for (a) 2004 and (b) 2013. Dashed line in each plot corresponds to the cone of influence. Origin of the X-axis corresponds to a start date of IPS observations for a given year.



### 4. Model Calculations

We examined temporal variations in the  $g$ -values when either SIR or CME arrived at the Earth by conducting model calculations using the following equation:

$$g^2 = \frac{1}{K} \int_0^\infty \Delta N_e^2 w(z) dz, \tag{4}$$

where  $w(z)$ ,  $z$ , and  $K$  are the weighting function of the IPS (Young, 1971), the distance along the line-of-sight, and a normalizing factor, respectively. This formula is valid for the weak-scattering region, i.e.,  $R > 0.2$  AU for 327 MHz. To calculate the  $g$ -value using Equation 4, information on the three-dimensional distribution of  $\Delta N_e$  must be given. In this study, we employed a simple model that prescribes the  $\Delta N_e$  distribution of either SIR or CME. The model includes the background and disturbance components; the spherically

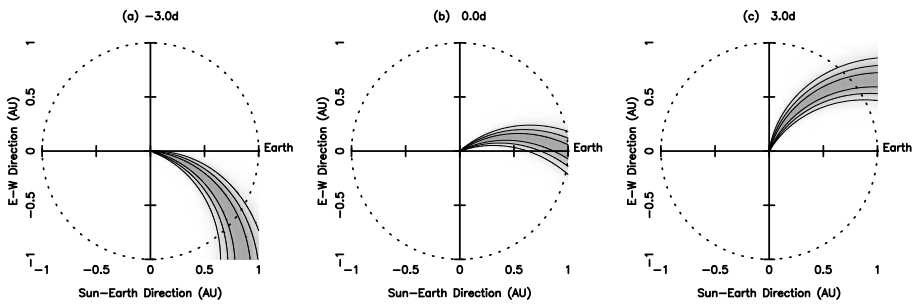


**Figure 13** Ecliptic cuts of the SIR model calculated for (a)  $-3.0$  days, (b)  $0.0$  days, and (c)  $+3.0$  days to the arrival time of the  $\Delta N_e$  peak at the Earth. Relative  $\Delta N_e$  values are indicated with a gray scale.

symmetrical distribution of  $\Delta N_e$  is assumed in the former, and either a spiral or a shell-shaped  $\Delta N_e$  distribution, which corresponds to SIR or CME, respectively, is assumed in the latter (see below). The inverse-square radial decrease of  $\Delta N_e$  is assumed for both background and disturbance components. Similar model calculations of CME were presented in previous studies (Tokumaru et al., 2000b, 2003, 2006a,b, Manoharan, 2006). In calculating  $w(z)$ , the apparent angular diameter of the radio source and the power-law index of the density-fluctuation spectrum are assumed to be 100 mas and  $-3.3$  (Kolmogorov value), respectively. The normalizing factor  $K$  is given by  $K = \int_0^\infty \Delta N_{e0}^2 w(z) dz$ , where  $\Delta N_{e0}$  denotes the background component of  $\Delta N_e$ . The model calculations performed here ignore the suppression effect by the weak-to-strong scattering transition and the radial evolution of the compression region by interaction with the background solar wind. This may result in overestimation of the increase in  $g$ -value for the near-Sun region.

#### 4.1. SIR Model

In the SIR model, we assumed a spiral-shaped corotating structure with a high  $\Delta N_e$ , as illustrated in Figure 13. The time of each plot is given as the difference from the time when the center of the SIR arrives at the Earth. In this model, we assumed a Gaussian-shaped increase whose peak is located at the equator, and the peak level of the  $\Delta N_e$  increase is set to be five times the quiet level. The e-folding latitude and longitude widths of the high  $\Delta N_e$  region are  $30^\circ$  and  $10^\circ$ , respectively. According to a comparison between IPS observations and model calculations, the enhanced scintillation region associated with corotating streams is confined within latitudes less than  $40^\circ$  (Homuiner, 1973). The longitude width assumed here corresponds approximately to the typical duration of compression regions associated with SIR at 1 AU:  $\sim 1$  day (Grandin, Aikio, and Kozlovsky, 2019). The propagation speed of the high  $\Delta N_e$  region is assumed to be  $800 \text{ km s}^{-1}$ .

Figure 14 shows sky-projection maps of the  $g$ -values calculated using the SIR model for the time difference from (a–f)  $-5$  to  $+5$  days every two days. The center of each map corresponds to the location of the Sun. The figure clearly reveals the movement of increased  $g$ -value areas, which correspond to the SIR, from the east to the west of the Sun. The area of increased  $g$ -values in the sky map grows as the SIR approaches the Earth, and reaches a maximum at 0 days. We then determined the average calculated  $g$ -value  $G_{ave}$  for each day. Figure 15 shows the temporal variation of  $G_{ave}$  for  $\pm 10$  days before/after the arrival of SIR at the Earth. The average values  $G_{ave}$  show a broad peak centered at 0 days, suggesting that the maximum correlation between  $G_{ave}$  and  $\Delta N_e$  occurs at 0 days. The same result is

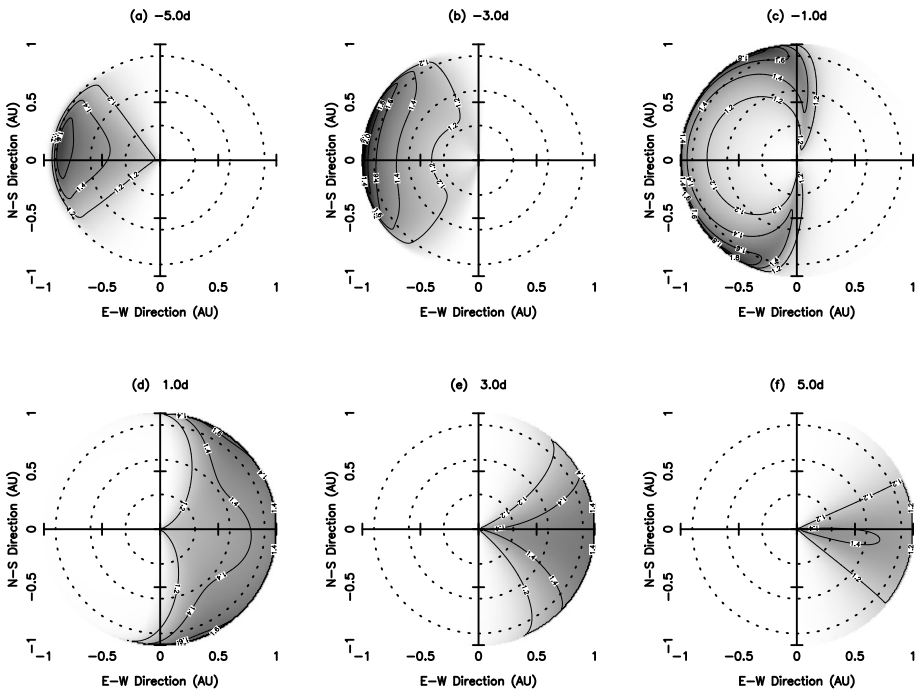


**Figure 14** Model calculations of the sky-projection map of  $g$ -values using the SIR model for (a)  $-5$  days, (b)  $-3$  days, (c)  $-1$  day, (d)  $+1$  day, (e)  $+3$  days, and (f)  $+5$  days to the arrival time of the  $\Delta N_e$  peak at the Earth. Center of the sky-projection map corresponds to the location of the Sun, and the dotted concentric circles are constant  $R$  contours drawn every  $0.3$  AU. Relative  $g$ -values are indicated with a gray scale.

expected for  $I_{50}$  and  $I_{hi}$ . This is consistent with the results of the comparison between the IPS indices and in situ data. However, the obtained result is inconsistent with model calculations performed in an earlier study (Homuiner, 1973), which showed double peaks in increased  $g$ -values a few days before and after the arrival of the corotating stream at the Earth. This discrepancy is attributed to the oversimplified model used in the earlier study, which ignores the thickness of the corotating stream and thereby the line-of-sight integration effects.

## 4.2. CME Model

Figure 16 illustrates the CME model calculated for three different points of time during propagation between the Sun and the Earth. The time, which is shown in the figure, denotes the difference from the time when the center of the CME arrives at the Earth. The CME model has a shell-shaped distribution of increased  $\Delta N_e$  that expands at a uniform speed. The expansion speed is assumed to be  $800 \text{ km s}^{-1}$ , and its center is located on the Sun–Earth line. The angular and radial profiles of the  $\Delta N_e$  increases are given by a Gaussian function with e-folding angular and radial widths of  $30^\circ$  and  $0.05$  AU, respectively. The  $\Delta N_e$  level at the center of the CME is assumed to be five times larger than the quiet level.

Figure 17 shows the sky-projection maps of calculated  $g$ -values and the radial profile of the maximum level for (a)  $-1.6$ , (b)  $-0.8$ , and (c)  $-0.1$  days with respect to the arrival time of the CME at the Earth. Since the CME is directed to the Earth in this model, the area of increased  $g$ -values is halo shaped in the upper panels of the figure. This increase becomes

**Figure 15** Calculated  $G_{ave}$  plotted as a function of the time difference to arrival of the  $\Delta N_e$  peak at the Earth.

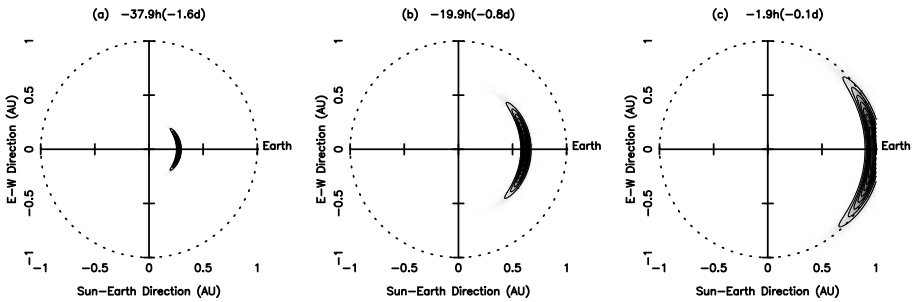
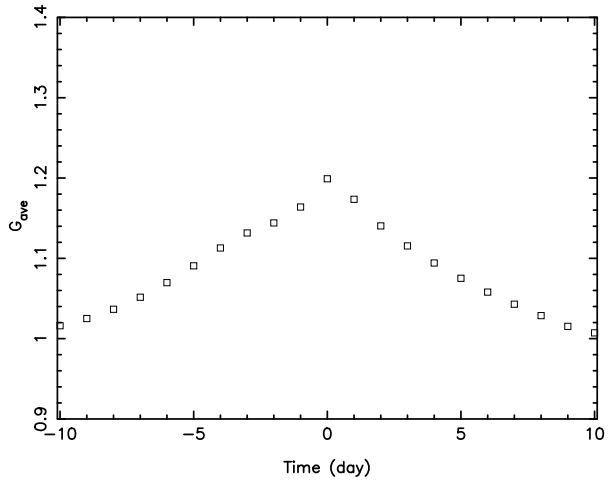


**Figure 16** Ecliptic cuts of the CME model for (a)  $-1.6$  days, (b)  $-0.8$  days, and (c)  $-0.1$  days to the arrival time of the  $\Delta N_e$  peak at the Earth. Relative  $\Delta N_e$  values are indicated by a gray scale. The center and right edge of the plot correspond to the locations of the Sun and the Earth, respectively.

stronger as the CME approaches the Earth, as shown in the lower panel. The peak values of increased  $g$ -values are plotted in Figure 18 as a function of the time difference to the arrival of CME’s central portion at the Earth. A sharp rise in the peak values at the Earth is demonstrated in the figure. This intensification of increase in  $g$ -value is ascribed to the line-of-sight integration effect. The largest contribution to the  $g$ -value comes from the solar wind near the Earth when the solar-elongation angle is close to  $90^\circ$ , i.e.,  $R \simeq 1$  AU, due to the inverse-square radial decrease of  $\Delta N_e$ . This result means that the greatest increase in  $g$ -value occurs when the CME arrives at the Earth and is consistent with the result obtained from a comparison between the IPS indices and in situ data.

This conclusion is similar to the case of SIR; however, it should be noted that the increases in  $g$ -values associated with CME are short lived compared to those associated with SIR. Although their duration depends on the expansion speed of the CME, the increases in  $g$ -value are only observed one or two days prior to the arrival of CME at the Earth, as shown in Figure 17. In contrast, the effect of SIR is likely to last for several days before and after the arrival of SIR at the Earth, as shown in Figure 15. The duration of the SIR effect does not depend on the solar-wind speed, but on the solar rotation. We also note that the intensification of the increase in  $g$ -value does not occur at  $\sim 1$  AU if a CME is not directed towards

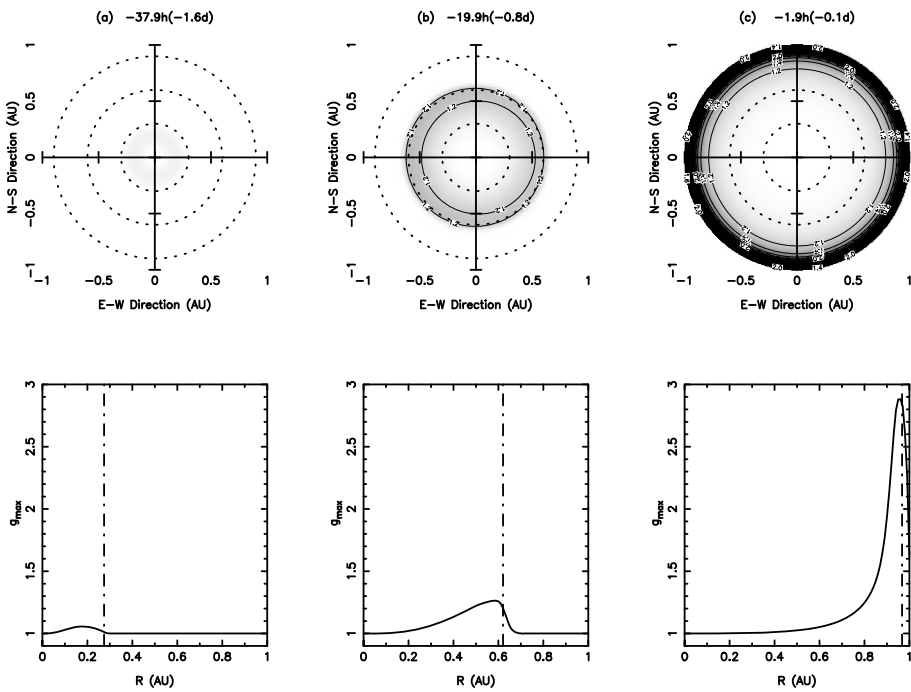


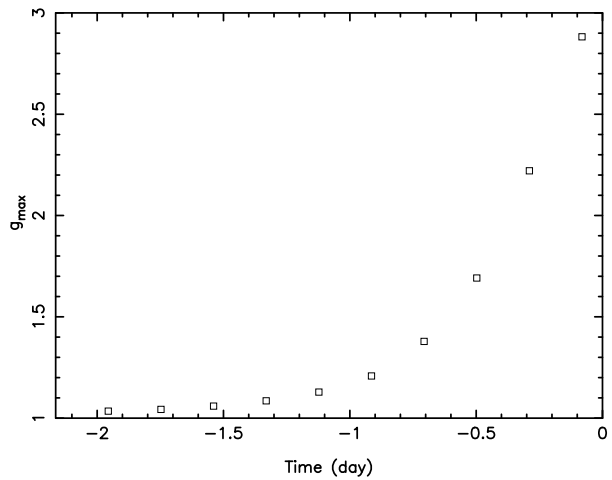
**Figure 17** (upper) Sky-projection maps and (lower) radial profiles of  $g$ -values calculated using the CME model for (a)  $-1.6$  days, (b)  $-0.8$  days, and (c)  $-0.1$  days to the arrival time of the  $\Delta N_e$  peak at the Earth. The center of the sky-projection map corresponds to the location of the Sun, and the dotted concentric circles are constant  $R$  contours drawn every  $0.3$  AU. Relative  $g$ -values are indicated by a gray scale in the sky-projection map. Maximum values of calculated  $g$ -values  $g_{max}$  at a given radial distance are plotted in the lower panel. Dot-dashed line in the lower plot indicates the location of the  $\Delta N_e$  peak.

the Earth because the central portion of the CME is not located where the local  $\Delta N_e$  level has the greatest effect on the  $g$ -value. In this case, in situ measurements near the Earth are probably incapable of detecting CME signatures; therefore, the case of non-Earth directed CMEs does not alter the above conclusion. The peak in increased  $g$ -values calculated with the CME model is much greater than that calculated with the SIR model, particularly at  $\sim 1$  AU. The reason for this is that, compared to the spiral-shaped region in the SIR model, the shell-shaped high- $\Delta N_e$  region assumed in the CME model intersects the line-of-sight over a longer length for large solar-elongation angles.

### 5. Summary and Discussion

We derived three types of IPS indices:  $I_{50}$ ,  $I_{hi}$ , and  $G_{ave}$ , which represent the  $\Delta N_e$  level of the inner heliosphere, from ISEE IPS observations over the years 1997–2019, and compared them with in situ observations near the Earth and geomagnetic Dst indices. No statistically significant difference in performance was found between  $I_{50}$ ,  $I_{hi}$ , and  $G_{ave}$ . The results indicated weak but significant positive correlations between the IPS indices and the solar-wind density, with a peak at day  $\tau = 0$  throughout the analysis period, as well as smaller correlation coefficients for SC24 than for SC23. Similar positive correlations were also found

**Figure 18** Peak values of  $g_{max}$  plotted as a function of the time difference to arrival of the  $\Delta N_e$  peak at the Earth.



between the IPS indices and  $dV/dt$  at  $\tau = 0$  day for both cycles. These results suggest that the IPS indices may indicate the occurrence of the compression region associated with the SIR or CME at the Earth, and are consistent with model calculations of the  $g$ -values performed in this study. Our findings are generally consistent with those from earlier studies using Cambridge IPS observations (Harrison et al., 1992; Lucek, Clark, and Moore, 1996), with some differences; for example, those studies reported a better correlation with the solar-wind density, whereas no evidence was found for any correlation with solar-wind speed. According to our results, the coefficients of significant correlations between the IPS indices and solar-wind speed were positive at  $\tau > 0$  for SC23 but negative at  $\tau < 0$  for SC24. Such complex behavior may account for the lack of correlation with the wind speed observed in the earlier study. The stronger correlation with solar-wind density revealed in the earlier study may be attributed to the greater level of solar activity during the analysis period, i.e., the SC22 maximum. According to a comparison between the IPS and Dst indices, significant negative correlations occurred at  $\tau > 1$  day, particularly for SC23, which is generally consistent with the findings of earlier studies comparing IPS indices with Ap indices (Harrison et al., 1992; Lucek, Clark, and Moore, 1996). However, it should be noted that the correlations obtained in this study are too weak for reliable predictions of solar-wind or geomagnetic disturbances. Possible reasons for these weak correlations are addressed below. The degree of positive or negative correlation, which is considered to depend on the distinctness of the solar-wind disturbances, tends to increase at solar maxima, with weaker correlations observed for SC24. Stronger correlations at the solar maxima are attributed to the increased occurrence of intense solar-wind disturbances, with the weaker correlations for SC24 ascribed to the decline in solar activity.

One of the potential reasons for the weak correlations is that the IPS indices are global parameters representing the average  $\Delta N_e$  level over a wide area of the inner heliosphere, whereas in situ and geomagnetic data represent local conditions at the Earth. A better correlation may be expected by selecting  $g$ -value data for large solar elongation. Nevertheless, information on the solar wind over a wide area is still included in the IPS indices because IPS observations represent the integration of solar-wind parameters along the line-of-sight. In earlier studies using Cambridge IPS observations, the correlation between the IPS and Ap indices was examined by sorting  $g$ -value data into three solar-elongation bands; however, no significant improvement of the maximum correlation coefficient was gained for the band

with large solar elongation (Harrison et al., 1992; Lucek, Clark, and Moore, 1996). Moreover, if data at large solar elongation were selected, the number of  $g$ -values would become too small to produce a statistically meaningful result from ISEE IPS observations, due to the limited number of observed sources. Thus, a computer-assisted tomography study of IPS observations with abundant lines-of-sight may be useful for improving the correlation between IPS and in situ observations (Kojima et al., 2007; Jackson et al., 2011; Tokumaru et al., 2021). The accuracy of the tomographic analysis depends on the amount of data; therefore, a high-sensitivity radio telescope that enables IPS observations for many radio sources per day is required for an accurate comparison with in situ observations. A global network of IPS observations is also important for improving tomographic analysis, particularly for transient heliospheric features, such as CMEs (e.g., Tokumaru et al., 2019; Jackson et al., 2022).

Another reason for the weak correlations may be the complex relationship between  $\Delta N_e$  and the solar-wind bulk density or speed. By convention,  $\Delta N_e$  derived from IPS observations is used as a proxy for the solar-wind density, and the proportionality between  $\Delta N_e$  and solar-wind density has served well as a first-order approximation in past studies (e.g., Hewish, Tappin, and Gapper, 1985; Tappin, 1986). However, according to the comparison between IPS observations and in situ measurements,  $\Delta N_e$  increases were not as large as those of bulk density (Ananthkrishnan, Coles, and Kaufman, 1980). Therefore, it is likely that the actual relationship between  $\Delta N_e$  and the solar-wind parameters is more complicated. The physical properties of  $\Delta N_e$ , i.e., solar-wind microturbulence are poorly understood; thus, further study is required to extract accurate information on the solar wind from IPS observations. Furthermore, the weak correlation between the IPS and Dst indices is partly attributed to the effect of the IMF Bz component, which strongly controls the occurrence of geomagnetic storms. The earlier study demonstrated that higher values of Ap occur preferentially in data associated with southward Bz (Hapgood and Harrison, 1994). Hence, an improved correlation between IPS and geomagnetic indices may be obtained by selecting southward Bz events, although this is beyond the scope of this study.

In this study, we determined long-term variations in the occurrence rates of solar-wind disturbances (including SIR/CIR and CME) during 1997–2019 using IPS indices. The occurrence rates derived in this study clearly exhibit solar-cycle dependence. That is, more solar-wind disturbances occurred at the SC23 maximum, SC 23/24 minimum, and SC24/25 minimum. The temporal variations in the occurrence rates are generally consistent with the combined effects of SIR/CIR and CME; however, this cannot account for the high occurrence rate observed in 2009, which may be ascribed to the fact that IPS observations provide information on the solar wind out of the ecliptic plane as well as the in-ecliptic plane. Therefore, a further study is needed to identify a solar source for the high occurrence rate observed in 2009. A periodicity of one complete or one-half solar-rotation period, which is considered as a signature of the CIR, was observed in the declining and rising phases according to the wavelet analysis of the IPS indices. This finding is generally consistent with the development of low-latitude coronal holes during those periods, although their solar-cycle maxima occurred in the declining phase (Fujiki et al., 2016). Thus, this study reveals that IPS indices are a useful tool for studying the long-term characteristics of solar-wind disturbances.

**Acknowledgments** The IPS observations were conducted under the solar-wind program at the Institute for Space-Earth Environmental Research (ISEE) of Nagoya University. We acknowledge the use of the OMNI-Web service and OMNI data of the NASA/GSFC Space Physics Data Facility. We thank the World Data Center C2 of Kyoto University and the geomagnetic observatories (Kakioka, Honolulu, San Juan, and Hermanus) for providing the Dst-index data. We also thank the WDC-SILSO, Royal Observatory of Belgium, for providing sunspot-number data. This research was partially supported by a JSPS KAKENHI Grant-in-Aid for Scientific Research (C) (21K03640).



**Author contributions** Munetoshi Tokumaru wrote the main manuscript text and prepared all figures. Ken'ichi Fujiki and Kazumasa Iwai discussed the results. All authors reviewed the manuscript.

**Data Availability** IPS data are publicly available from the ISEE web site (<https://stsw1.isee.nagoya-u.ac.jp/vlist>). OMNI, Dst-index, and sunspot-number data are publicly available from the OMNIWeb service (<https://omniweb.gsfc.nasa.gov/>), the World Data Center of Kyoto University (<https://wdc.kugi.kyoto-u.ac.jp/index.html>), and the WDC-SILSO (<https://www.sidc.be/silso/>), respectively. The IPS indices used in the current study are available from the corresponding author on reasonable request.

## Declarations

**Competing interests** The authors declare no competing interests.

**Open Access** This article is licensed under a Creative Commons Attribution 4.0 International License, which permits use, sharing, adaptation, distribution and reproduction in any medium or format, as long as you give appropriate credit to the original author(s) and the source, provide a link to the Creative Commons licence, and indicate if changes were made. The images or other third party material in this article are included in the article's Creative Commons licence, unless indicated otherwise in a credit line to the material. If material is not included in the article's Creative Commons licence and your intended use is not permitted by statutory regulation or exceeds the permitted use, you will need to obtain permission directly from the copyright holder. To view a copy of this licence, visit <http://creativecommons.org/licenses/by/4.0/>.

## References

- Allen, R.C., Ho, G.C., Mason, G.M., Li, G., Jian, L.K., Vines, S.K., et al.: 2021, *Geophys. Res. Lett.* **48**, e91376. DOI.
- Ananthakrishnan, S., Coles, W.A., Kaufman, J.J.: 1980, *J. Geophys. Res.* **85**, 6025. DOI.
- Besliu-Ionescu, D., Maris Muntean, G., Dobrica, V.: 2022, *Solar Phys.* **297**, 65. DOI.
- Chashei, I.V., Tyul'bashev, S.A., Shishov, V.I., Subaev, I.A.: 2016, *Space Weather* **14**, 682. DOI.
- Coles, W.A.: 1978, *Space Sci. Rev.* **21**, 411. DOI.
- Fujiki, K., Tokumaru, M., Hayashi, K., Satonaka, D., Hakamada, K.: 2016, *Astrophys. J.* **827**, L41. DOI.
- Gapper, G.R., Hewish, A., Purvis, A., Duffett-Smith, P.J.: 1982, *Nature* **296**, 633. DOI.
- Gerontidou, M., Mavromichalaki, H., Daglis, T.: 2018, *Solar Phys.* **293**, 131. DOI.
- Gosling, J.T., Pizzo, V.J.: 1999, *Space Sci. Rev.* **89**, 21. DOI.
- Grandin, M., Aikio, A.T., Kozlovsky, A.: 2019, *J. Geophys. Res.* **124**, 3871. DOI.
- Hapgood, M., Harrison, R.: 1994, *Geophys. Res. Lett.* **21**, 637. DOI.
- Harrison, R.A., Hapgood, M.A., Moore, V., Lucek, E.A.: 1992, *Ann. Geophys.* **10**, 519.
- Hewish, A., Scott, P.F., Wills, D.: 1964, *Nature* **203**, 1214. DOI.
- Hewish, A., Tappin, S.J., Gapper, G.R.: 1985, *Nature* **314**, 137. DOI.
- Houminer, Z.: 1971, *Nat. Phys. Sci.* **231**, 165. DOI.
- Houminer, Z.: 1973, *Planet. Space Sci.* **21**, 1617. DOI.
- Jackson, B.V., Hick, P.P., Buffington, A., Bisi, M.M., Clover, J.M., Tokumaru, M., Kojima, M., and, F.K.: 2011, *J. Atmos. Solar-Terr. Phys.* **73**, 1214. DOI.
- Jackson, B.V., Tokumaru, M., Fallows, R.A., Bisi, M.M., Fujiki, K., Chashei, I., Tyul'bashev, S., Chang, O., Barnes, D., Buffington, A., Cota, L., Bracamontes, M.: 2022, *Adv. Space Res.* DOI. in press.
- Jian, L.K., Russell, C.T., Luhmann, J.G., Skoug, R.M., Steinberg, J.T.: 2008, *Solar Phys.* **249**, 85. DOI.
- Kojima, M., Kakinuma, T.: 1990, *Space Sci. Rev.* **53**, 173. DOI.
- Kojima, M., Tokumaru, M., Fujiki, K., Hayashi, K., Jackson, B.V.: 2007, *Astron. Astrophys. Trans.* **26**, 467. DOI.
- Lucek, E.A., Rodger, A.S.: 1995, *Ann. Geophys.* **13**, 1237.
- Lucek, E.A., Clark, T.D.G., Moore, V.: 1996, *Ann. Geophys.* **14**, 139. DOI.
- Manoharan, P.K.: 1997, *Geophys. Res. Lett.* **24**, 2623. DOI.
- Manoharan, P.K.: 2006, *Solar Phys.* **235**, 345. DOI.
- Manoharan, P.K.: 2010, *Solar Phys.* **265**, 137. DOI.
- Richardson, I.G., Cane, H.V.: 2010, *Solar Phys.* **264**, 189. DOI.
- Richardson, I.G.: 2018, *Living Rev. Solar Phys.* **15**, 1. DOI.
- Sugiura, M.: 1964, *Annual International Geophysical Year* **35**, Pergamon, New York, 9.
- Tappin, S.J., Hewish, A., Gapper, G.R.: 1984, *Planet. Space Sci.* **32**, 1273. DOI.



- Tappin, S.J.: 1986, *Planet. Space Sci.* **34**, 93. DOI.
- Tokumaru, M., Kojima, M., Ishida, Y., Yokobe, A., Ohmi, T.: 2000a, *Adv. Space Res.* **25**, 1943. DOI.
- Tokumaru, M., Kojima, M., Fujiki, K., Yokobe, A.: 2000b, *J. Geophys. Res.* **105**, 10435. DOI.
- Tokumaru, M., Kojima, M., Fujiki, K., Yamashita, M., Yokobe, A.: 2003, *J. Geophys. Res.* **108**, 1220. DOI.
- Tokumaru, M., Kojima, M., Fujiki, K., Yamashita, M., Baba, D.: 2005, *J. Geophys. Res.* **110**, A01109. DOI.
- Tokumaru, M., Yamashita, M., Kojima, M., Fujiki, K., Nakagawa, T.: 2006a, *Adv. Space Res.* **38**, 547. DOI.
- Tokumaru, M., Kojima, M., Fujiki, K., Yamashita, M.: 2006b, *Nonlinear Process. Geophys.* **13**, 329. DOI.
- Tokumaru, M., Kojima, M., Fujiki, K., Yamashita, M., Jackson, B.V.: 2007, *J. Geophys. Res.* **112**, A05106. DOI.
- Tokumaru, M., Kojima, M., Fujiki, K., Maruyama, K., Maruyama, Y., Ito, H., et al.: 2011, *Radio Sci.* **46**, RS0F02. DOI.
- Tokumaru, M.: 2013, *Proc. Japan Acad. Ser. B* **89**, 67. DOI.
- Tokumaru, M., Fujiki, K., Iwai, K., Tyul'bashev, S., Chashei, I.: 2019, *Solar Phys.* **294**, 87. DOI.
- Tokumaru, M., Fujiki, K., Kojima, M., Iwai, K.: 2021, *Astrophys. J.* **922**, 73. DOI.
- Tsurutani, B.T., Goldstein, B.E., Gonzales, W.D., Tang, F.: 1988, *Planet. Space Sci.* **36**, 205. DOI.
- Tsurutani, B.T., Lakhina, G.S., Hajra, R.: 2020, *Nonlinear Process. Geophys.* **27**, 75. DOI.
- Young, A.T.: 1971, *Astrophys. J.* **168**, 543. DOI.
- Zwickl, R.D., Doggett, K.A., Sahn, S., Barrett, W.P., Grubb, R.N., Detman, T.R., et al.: 1998, *Space Sci. Rev.* **86**, 633. DOI.

**Publisher's Note** Springer Nature remains neutral with regard to jurisdictional claims in published maps and institutional affiliations.

Springer Nature or its licensor (e.g. a society or other partner) holds exclusive rights to this article under a publishing agreement with the author(s) or other rightsholder(s); author self-archiving of the accepted manuscript version of this article is solely governed by the terms of such publishing agreement and applicable law.